RSC Advances

This is an *Accepted Manuscript*, which has been through the Royal Society of Chemistry peer review process and has been accepted for publication.

Accepted Manuscripts are published online shortly after acceptance, before technical editing, formatting and proof reading. Using this free service, authors can make their results available to the community, in citable form, before we publish the edited article. This *Accepted Manuscript* will be replaced by the edited, formatted and paginated article as soon as this is available.

You can find more information about *Accepted Manuscripts* in the Information for Authors.

Please note that technical editing may introduce minor changes to the text and/or graphics, which may alter content. The journal's standard Terms & Conditions and the Ethical guidelines still apply. In no event shall the Royal Society of Chemistry be held responsible for any errors or omissions in this *Accepted Manuscript* or any consequences arising from the use of any information it contains.

ROYAL SOCIETY OF CHEMISTRY

www.rsc.org/advances

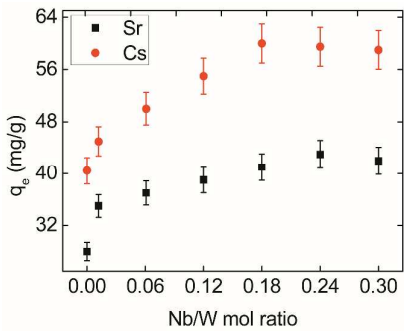

Adsorption capacity of Sr^{2+} and Cs^{+} onto hexagonal tungsten oxide was enhanced by incorporation of Nb.

RSC Advances Accepted Manuscript

Enhancing Adsorption Capacity of Sr^{2+} and Cs^{+} onto Hexagonal Tungsten Oxide by Doped Niobium

Bijun Liu, Wanjun Mu, Xiang Xie, Xingliang Li, Hongyuan Wei, Zhaoyi Tan, Yuan Jian, Shunzhong Luo

Institute of Nuclear Chemistry and Physics, China Academy of Engineering Physics, Mianyang, 621900, China

Corresponding should write to

Xingliang Li

Institute of Nuclear Chemistry and Physics, China Academy of Engineering Physics

64 Mianshan Road, Mianyang, 621999, Sichuan Province, China

Tel: +86 816 2494854

Fax: +86 816 2495280

E-mail: xingliang@caep.cn

Shunzhong Luo

Institute of Nuclear Chemistry and Physics, China Academy of Engineering Physics

64 Mianshan Road, Mianyang, 621999, Sichuan Province, China

Tel: +86 816 2484241

Fax: +86 816 2495280

E-mail: luoshzh@caep.cn

RSC Advances Accepted Manuscript

Abstract: Large amounts of radioactive waste effluents are produced by the nuclear industry each year and more efficient methods are required for their treatment to decrease final disposal costs and environmental discharges. Among various methods, adsorption stands out as a relatively clean and energy-efficient separation method. Hexagonal tungsten oxide (hex-WO_3) has potential application to deal with acidic radioactive waste. To extend the adsorption capacity of hex-WO_3, extensive series of Nb-doped WO_3 were hydrothermal synthesized. Incorporation of Nb into WO_3 framework will lead to expansion of layer spacing and be accompanied by exclusion of guest water. Comparing to bare hex-WO_3, adsorption capacity of Sr^{2+} on Nb-doped WO_3 is markedly improved and the Cs^+ adsorption capacity is not obstructed.

Key words: adsorption; hexagonal tungsten oxide; radioactive waste; Sr^{2+} ion, Cs^+ ion

RSC Advances Accepted Manuscript

1 Introduction

Nuclear energy increasingly represents an important option for generating clean CO_2-free electricity [1]. Most of the highly nuclear-dependent countries have affirmed their plans to continue development of nuclear power after the Fukushima accident. To ensure a safe and sustainable development of nuclear energy, the challenges of effectively dealing with radioactive waste must be addressed. A concept of closing the fuel cycle has been developed for reducing the volume and the long-term risk of spent fuel by advanced reprocessing technologies. Currently, reprocessing of used nuclear-fuel is carried out in several countries including France, UK, Russia and Japan using the PUREX (Plutonium and Uranium Extraction) process. At the same time, it may also be possible to separate heat-generating fission products present in used nuclear-fuel. ^{137}Cs and ^{90}Sr, with half-lives of 28.9 years and 30.1 years respectively, contribute a large part of the heat load and radiation in high level waste. Thus, separation of ^{137}Cs and ^{90}Sr from used fuel waste is a topical area of research.

Removal of ^{90}Sr and ^{137}Cs from waste provides several advantages for the final treatment of nuclear wastes. By eliminating most of the heat generation and radiation, it can greatly reduce the waste volume and thereby save the repository capacity. Besides, removal of ^{90}Sr and ^{137}Cs can facilitate the handling and transportation of high radioactive waste, either for subsequent reprocessing or for direct disposal. A variety of methods, including solvent extraction, adsorption, precipitation, coagulation, electrochemical, and membrane processes, have been developed for the removal of ^{137}Cs and ^{90}Sr from radioactive waste. Among those methods, solvent extraction and adsorption are used widely. Solvent extraction provides the benefits such as its convenience in combining with PUREX processes and high flexibility in stage designing. Current commercial nuclear-separation technology is based upon solvent-solvent extraction, but this technology suffers complications due to radiation-induced decomposition of organic molecule. Consequently, new separation methodologies are being searched for. At same time, it is well known that inorganic adsorbents present very good stability against high radiation levels. Once sorption has occurred, the solid-matrix material can be converted to a waste form suitable for safe disposal. The strategy that concentrating the bulk of radioactive effluent onto a small volume of inorganic sorbent offer a simple, safe and economical alternative to current solvent extraction separation technologies. A

RSC Advances Accepted Manuscript

wide range of inorganic materials have been investigated for this application over the past decades, such as zeolite[2], metal sulfide[3, 4], silicotitanate [5, 6], titanate nanofibers[7], antimony pyrochlore[8], and other hybrid materials[9]. However, the acidity of the waste solution is a limiting factor in the use of inorganic adsorbents available today. Because most uranium fuels are often dissolved by concentrated HNO_3 solution, waste effluents are usually strong nitric acid solutions. On the other hand, some materials that display selectivity for Sr^{2+} in highly acidic solutions, such as antimony pyrochlore, are generally not selective for Cs^+ [10]. Others, such as the hexacyanoferrates [9, 11] and zirconium molybdopyrophosphate [12, 13] show selectivity for Cs^+ in acid solutions, but these materials have no selectivity for Sr^{2+}. The material that is selective both for both ^{90}Sr and ^{137}Cs in strongly acidic media do not yet appear to exist.

The advantage that a single material adsorbs multiple radioactive nuclides is simplicity in disposing of radioactive material. There would be only a single waste stream to be produced once it is saturated with radioactivity. To address this complex mix of requirements, an absorbent with high selectivity both for Sr^{2+} and Cs^+ in acidic solution would find almost immediate application in radioactive treatment.

Hexagonal tungstate oxide (hex-WO_3) has attracted much attention owing to its well-known tunnel structure [14]. In the WO_3 hexagonal structure, the octahedra form six-membered rings in the equatorial plane (001) and the stacking of such planes along the c-axis leads to the formation of large tunnels. The tunnel structure gives the material the ability to host ions (such as NH_4^+, Li^+, Na^+, etc.)[15]. The guest ions occupy the positions in the “hexagonal window” tunnels between the layers, and these cations can be exchanged. Furthermore, hex-WO_3 is very stable in acidic solution. This implies that hex-WO_3 can be used as adsorbent to remove radionuclides from acidic radioactive waste [16, 17]. Recently, Griffith and Luca reported that microporous tungstates display promising distribution coefficients for both Cs^+ and Sr^{2+} cations in acidic radioactive waste [18, 19]. However, the adsorption capacity of Sr^{2+} is relative lower than that of Cs^+.

One strategy for modulating the ion selectivity is the insertion of heteroatoms into the framework W^{6+} sites thereby possibly affecting channel dimensionality and acidity of the adsorption sites. It was well known that Nb and W have similar coordination chemistry and atomic scattering factors. It might be suggested that W can be replaced by Nb, according to stoichiometry

RSC Advances Accepted Manuscript

of hexagonal tungsten bronze, i.e. M ($Nb^{5+}W^{6+}$)O_3 (wherein the "M" cation resides)[20-22]. In general terms, adsorption selectivity of a porous material is determined by a combination of ion or molecule sorption to pore, chemical bonding inside of pore, and surface interactions between ion/molecule and solvent. The introduction of lower valence cation will lead to expansion of the negative charge of hex-WO_3 framework, and further impart selectivity through channel size and surface charge. This could strengthen host-gust static interaction of noumenal tungstate framework and extraframework cations, and then to enhance the adsorption capacity.

Here, we are investigating a methodology of enhancing adsorption capacity of Sr^{2+} and Cs^{+} onto hexagonal hex-WO_3 microcrystal by doped niobium. To explore the possibility of utilizing Nb-doped WO_3 to removal of ^{90}Sr and ^{137}Cs from acidic waste, the adsorption kinetics of Sr^{2+} and Cs^{+} on the Nb-doped WO_3 was analyzed by fitting various kinetic models. Experimental equilibrium data were fitted to the Langmuir and Freundlich isotherm equations to determine the best-fit isotherm equation.

2 Experiment

2.1 Nb-doped hex-WO_3 synthesis

All chemicals used were purchased and used without further purification. $NbCl_5$ was dissolved in dry ethanol as Nb precursor. Sodium tungstate dihydrate ($NaWO_4{\cdot}2H_2O$) with different Nb mole ratios was mixed in 45 mL of distilled water under uninterrupted stirring at room temperature. HCl (5 mL at 3 $mol{\cdot}L^{-1}$) and $(NH_4)_2SO_4$ (30 mL at 0.5 $mol{\cdot}L^{-1}$) solution were added in succession. The mixture was transferred to a 100 mL polytetrafluoroethylene-coated stainless steel autoclave. The autoclave was sealed and heated at 170°C in a furnace for 24 h, then cooled to room temperature. The resulting light-green precipitate was collected by filtration and washed with distilled water to remove any residual ions. The powder was then freeze-dried under vacuum for 12 h.

2.2 Characterization

Phase characterization was carried out using X-ray diffraction (XRD) (X'Pert PRO, PANalytical, Almelo, Netherlands) with Cu-*Ka* radiation (λ = 0.15406 nm at 40 kv and 45 mA).

RSC Advances Accepted Manuscript

The shapes of the products were observed with a field emission scanning electron microscope (FE-SEM Philips XL30 FEG, Eindhoven, Netherlands). Nitrogen adsorption and desorption isotherms were measured at 77 K with a Beckman Coulter SA 3100 surface area analyzer. To determine the surface area, the BET method was used. Fourier transform infrared (IR) spectra were recorded from KBr disks using a Nicolet 5700 spectrophotometer (Thermo Electron Corporation, USA), with a resolution of 2 cm^{-1} and operating range of 400–4000 cm^{-1} using OMNIC software. Zeta Meter (ZetaPALS, BLK, USA) was applied to measure the zata potential. Ultraviolet-visible (UV-vis) diffuse reflectance spectra of samples were obtained using a Lambda 850 (PerkinElmer, USA) double-beam spectrophotometer, which was equipped with an integrating sphere attachment, using the reflectance of $BaSO_4$ as a reference. XPS measurements were conducted using a Physical Electronics ESCA 5600 spectrometer with a monochromatic Al K*a* X-ray source at a power of 200W/14kv and a multi-channel detector (Omni IV). Narrow high-resolution scans were run with pass energy of 40 eV, dwell time of 250 ms, and step size of 0.1 eV. The C(1s) peak at 284.8 eV was used as the internal reference for the absolute binding energy. Gaussian-Lorentzian curves and Shirley background were applied for photoelectron peak analysis.

2.3 Adsorption capability

To determine the pH range at which the maximum adsorption of Cs^+ or Sr^{2+} ions would take place, adsorbent (0.2 g) was added to a series of 100 mL solutions containing Cs^+ and Sr^{2+} ions with a desired concentration. The initial acidity was adjusted to values ranging from $[HNO_3]$=1.0 to pH=7.0 using dilute solution of HNO_3 or NaOH. The suspension was agitated at 298 K to attain equilibrium. The suspension obtained was centrifuged to separate the solid from the liquid phase. The clear liquid phases obtained were diluted to an appropriate concentration range for the elemental analysis using Atomic Absorption Spectrophotometer (AAalyst800, PerkinElmer, USA). The amount of metal ions retained in the adsorbent q_e ($mg \cdot g^{-1}$) was calculated by:

$$q_e = \frac{(C_i - C_e)V}{W} \quad (1)$$

where C_i and C_e are the initial and equilibrium solution ions concentrations ($mg \cdot L^{-1}$), V is the

RSC Advances Accepted Manuscript

volume (mL) and W is the adsorbent weight (g).

Kinetic studies were performed at room temperature (298 K). For these investigations, WO_3 (0.2g) was contacted with 100 mL solution containing known concentration of Cs^+ and Sr^{2+} ions and the solution in the container was kept stirred in a thermostat shaker. The concentration of Cs^+ and Sr^{2+} ions was determined as a function of time. The amount of ion adsorbed at a time t, q_t ($mg \cdot g^{-1}$), was calculated using equation (2):

$$q_t = \frac{(C_i - C_t)V}{W} \tag{2}$$

where C_i and C_t are the initial and t time concentrations($mg \cdot L^{-1}$) of metal ion in solution. Pseudo-first-order and pseudo-second-order kinetic models are used to investigate adsorption processes[23]. The pseudo-first-order model can be written as follows:

$$\frac{dq_t}{dq_e} = k_1(q_e - q_t) \tag{3}$$

where k_1 is the pseudo-first-order rate constant (min^{-1}). Integrating Eq. (3) with the initial condition $q_t = 0$ at $t = 0$ gives:

$$\log(q_e - q_t) = \log q_e - \frac{k_1}{2.303}t \tag{4}$$

The pseudo-second-order adsorption kinetic rate equation is expressed as:

$$\frac{dq_t}{dq_e} = k_2(q_e - q_t)^2 \tag{5}$$

where k_2 is the adsorption rate constant. Where $q_t = 0$ at $t = 0$, then:

$$\frac{t}{q_t} = \frac{1}{k_2 q_e^{\ 2}} + \frac{1}{q_e}t \tag{6}$$

The model given by Boyd et al. is applied to identify the step governing the rate of removal from solution [24]:

$$F(t) = 1 - \frac{6}{\pi^2}\sum_{n=1}^{\infty}\frac{1}{n^2}\exp\left(-n^2 Bt\right) \tag{7}$$

where F is the fractional attainment of equilibrium at time t ($F = q_t/q_e$), B is the time constant and n is an integer (1, 2, 3, etc.). Procedures to obtain the value of Bt was provided elsewhere [24, 25].

RSC Advances Accepted Manuscript

To study the adsorption isotherms, adsorbent (0.2 g) was added to the solutions of Sr^{2+} and Cs^{+}, and their pH values were adjusted to 4. The suspension was treated in a thermostatically controlled agitator at 298 K to attain equilibrium. Solutions were then centrifuged and concentrations of Cs^{+} and Sr^{2+} were determined. The quantity of adsorbed ions was calculated as the difference between the initial and final concentrations at equilibrium. The Langmuir and Freundlich isotherm models are used to fit the adsorption isotherm data. The Langmuir equation is expressed as:

$$q_e = \frac{QbC_e}{1+bC_e} \tag{8}$$

where Q (mg·g^{-1}) is the maximum adsorption capacity, and b (L·mg^{-1}) is Langmuir equilibrium constant related to the energy of sorption. The Freundlich equation is an empirical adsorption model expressed as:

$$q_e = k_f C_e^{\frac{1}{n}} \tag{9}$$

where k_f is the Freundlich constant related to the sorption capacity, and n is the empirical constant.

In order to determine how well the resulting line fits the data, the sum of squares errors (SSE) is calculated as Eq. (10).

$$SSE = \sum \left[\frac{(q_{\exp} - q_{theo})}{q_{\exp}} \right]^2 \tag{10}$$

Where q_{exp} is the solid phase concentration determined at equilibrium (mg·g^{-1}), and q_{theo} is the corresponding value calculated from Langmuir or Freundlich model (mg·g^{-1}).

3. Results and discussion

3.1 Characterization of hex-WO_3 and Nb-doped hex-WO_3

XRD patterns of hex-WO_3 and Nb-doped WO_3 are shown in Fig. 1. The diffraction peaks of the materials without dopant in Fig. 1a can be readily indexed to the hex-WO_3 phase according to JCPDS card 33-1387 with lattice constants a = 7.30 Å, c = 3.90 Å and space group *P6mmm*. There is no any other phase or impurity in hex-WO_3 XRD pattern, indicating that hex-WO_3 with high

RSC Advances Accepted Manuscript

purity can be obtained by the method of hydrothermal synthesis. Nb-doped WO_3 can be considered to have a hexagonal tungsten bronze structure, since Nb and W have similar atomic scattering factors [26, 27]. The diffraction peak, near 22.30°, can be used to detect framework contraction or expansion (Fig. 1). This diffraction peak shifts from 22.34° (Fig. 1a) to 22.79° (Fig. 1f) upon incorporation of niobium into WO_3 with increase of Nb/W mole ratio from 0 to 0.24. The change indicates expansion of d_{001} spacing, which increases from 3.81 to 3.90 Å.

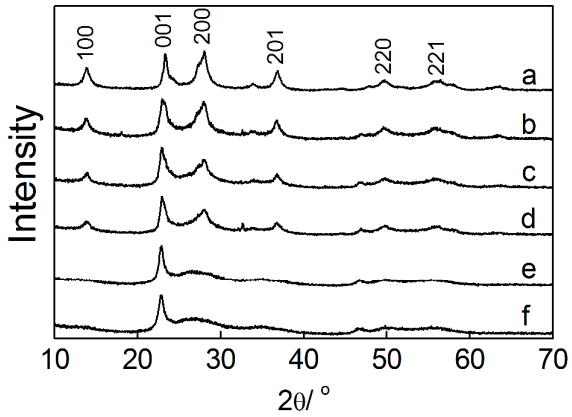

Figure 1 XRD patterns of WO_3 with Nb/W ratios of 0(a), 0.012(b), 0.061(c), 0.12(d), 0.18(e) and 0.24(f).

3.2 Particle morphology

The SEM images of the samples in Fig. 2 illustrate the interesting morphological changes of the solids by incorporating Nb with various percentages into WO_3. Bare hex-WO_3 is highly uniform fibril with lengths varying from 500 to 800 nm and diameters from 10 to15 nm (Fig. 2a). Particle morphology can be obtained with increase of the dopant amount of Nb (Fig. 2b and 2c). It has also been observed that a further increase of the Nb amount leads to a disappearance of the fiber structure (Fig. 2d). For example, the fiber phase will almost totally disappear when mole ratio of Nb/W reaches 0.24, and only agglomerate like particles are retained in products (Fig. 2d). So, the amount of dopant content is found to cause a change in the morphology as well as in the overall crystalline nature of the products.

RSC Advances Accepted Manuscript

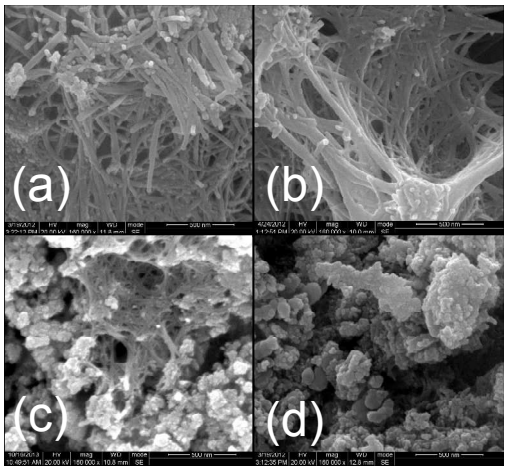

Fig. 2. SEM of WO_3 with Nb/W ratios of 0(a), 0.012(b), 0.18 (c) and 0.24 (d).

3.3 N_2 adsorption isotherms

In the following text, Nb-doped WO_3 refer the Nb/W mole ratio of 0.18. The nitrogen adsorption/desorption isotherms are presented in Fig. 3. The hex-WO_3 and the Nb-doped WO_3 exhibit a typical type-II isotherm and H3-type hysteresis loops, indicating a very wide distribution of pores size and shape. The hysteresis loop of Nb-doped WO_3 is very narrow, the adsorption and desorption branches being almost vertical and nearly parallel above 0.8 relative pressure, confirming the presence of a significant outer surface. As can be seen from SEM imagine, particle morphology of Nb-doped WO_3 is different from bare WO_3. The multi-point BET surface areas of Nb-doped WO_3 were evaluated to be 153 $m^2 \cdot g^{-1}$, which was much higher than pure hex-WO_3 (54 $m^2 \cdot g^{-1}$). We consider the particle size and morphology are main factor that might influence the surface areas.

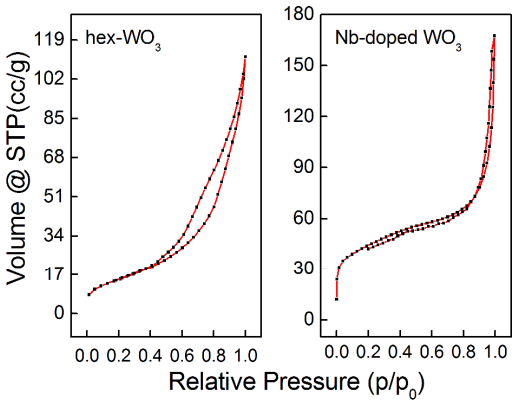

Figure 3 N_2 adsorption/desorption isotherms of WO_3

RSC Advances Accepted Manuscript

3.4 Analysis of IR Absorption spectroscopy

IR spectra of WO_3 are shown in Fig. 4. The existence of an intense and narrow band at 1620~1625 cm^{-1} indicates that structural water is coordinated as water molecules. The *v*(OH) vibration associated with this structural water makes a contribution to the broad band at 3150 cm^{-1}. The peak at 3150 cm^{-1} is disappear or very weak in Nd-doped WO_3, indicating the water exclusion. Peak at ~1400 cm^{-1} is assigned to *v*(OH) and δ(OH) of adsorbed water. At the same time, this peak can be also assigned to the stretching vibrations of NH_4^+. The guest ions in the channel of WO_3, such as Na^+, NH_4^+ and H_2O, are orientationally disordered and can be exchanged by other ions, such as K^+, Cs^+, et al [15]. After adsorption Cs^+ or Sr^{2+}, the much weaker intense of this peak indicates the molecular or ion responding to this peak can be exchanged by Cs^+ or Sr^{2+} ions. Peaks at 1189 and 1112 cm^{-1} are assigned to *v*(W=O). These peaks almost disappear in Nb-doped WO_3 (Fig. 4b), suggesting these functional groups have been changed after Nb-doped. However, the peaks of 1189 and 1112 cm^{-1} are still observed in Fig 4e and 3150 cm^{-1} peak appear in Fig. 4f, indicating the sites to occupy Cs^+ and Sr^{2+} ions are different. The broad peak at 790 cm^{-1} is assigned to the *v*(W–O_{inter}–W) of bridged corner-sharing WO_6 octahedron in hex-WO_3. It shifts to 831 cm^{-1} after incorporation of Nb into WO_3 framework. New peaks at 644, 559 cm^{-1} of Nb-doped WO_3 are assigned to *v*(O–W–O) that is within the *ab*-plane, suggesting that bridging O atoms play different roles within Nb-doped WO_3. The shifts of these peaks indicate that there are some changes of lengthen or angle of some W–O bands , which may be caused by the distortion of WO_6 octahedron after incorporation of Nb into WO_3 framework[20, 28, 29].

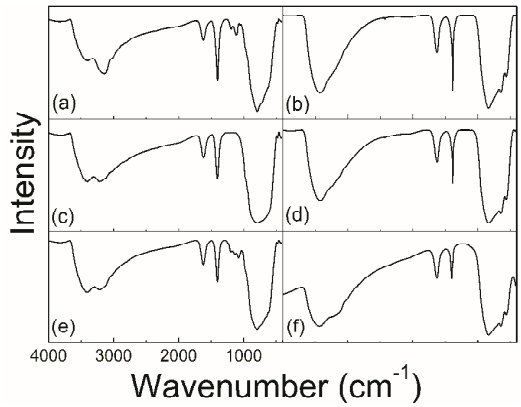

Fig. 4 IR patterns of WO_3 before and after sorption. hex-WO_3 (a), Nb-doped WO_3 (b), Cs

RSC Advances Accepted Manuscript

adsorbed hex-WO_3(c), Cs adsorbed Nb-doped WO_3(d), Sr adsorbed hex-WO_3(e), Sr adsorbed Nb-doped WO_3(f)

3.5 Analysis of UV-Visible Absorption Edge Energy

The optical absorption edge energies of samples were obtained from diffuse reflectance UV-vis spectra using following equation [30, 31]:

$$[F(R_\infty)hv]^{1/n} \propto (hv - E_o) \tag{11}$$

where hv is the energy of the incident photon and E_o is the optical absorption edge energy. The exponent n depends on the type of optical transition caused by photon absorption. An excellent fit was obtained using this method (n=2) for amorphous WO_3 sample. F (R_∞) is the so-called Kubelka-Munk function (Eq. 12), which is used to convert reflectance measurements (R_{sample}) into equivalent absorption spectra using the reflectance of reference ($R_{reference}$).

$$F(R_\infty) = \frac{(1-R_\infty)^2}{2R_\infty} \tag{12}$$

$$R_\infty = \frac{R_{sample}}{R_{reference}} \tag{13}$$

Then, a plot of $[F(R_\infty)\cdot hv]^{1/n}$ vs hv can be used to determine the absorption edge energy. The band-gap wavelength was taken to be the intersection of steep absorption edge line with a horizontal baseline corresponding to the maximum reflectance (Fig. 5). The nonlinear region found at energies lower than E_o is known as the Urbach tail, which is related to low-frequency acoustic modes that lead to fluctuations in the band gap [32].

The band gap of hex-WO_3 is determined to be 2.81 eV, which is in agreement with reported values for WO_3 of 2.70-3.25 eV. Compared with hex-WO_3, Nb-doped WO_3 show a blue shift of the absorbance edges (3.18 eV). This change might be attributed to the ligand to metal charge-transfer transition. In this transition, an electron is transferred from the highest occupied molecular orbital (HOMO), which has O_{2p} nonbonding orbital character, to the lowest unoccupied molecular orbital (LUMO), which is an antibonding orbital with W_{5d} orbital parentage. The incorporation Nb into WO_3 could lead to out-of-center distortions. Attributed to Jahn-Teller effects, this intra-octahedral distortion is the driving force to allow for a less strained coordination

RSC Advances Accepted Manuscript

environment around W [20, 33, 34]. Provided the MO_6 (M=Nb or W) octahedron are distorted from the ideal symmetry, the d_{xy}, d_{xz} and d_{yz} orbitals are differently destabilized. This overlap is more important between d_{xz} and d_{yz} with p-oxygen orbital because the M–O bond lengths are shorter and the orientations are more favorable [35]. As a consequence, the LUMO are always symmetry-adapted combinations of d_{xy}-like orbitals. These changes lead to the increase of the optical absorption edge energy. In addition, metal to metal charge-transfer transition also play an important role, which is a transfer of electrons from filled d-orbitals to empty d-orbitals. Compared with pristine phases, all samples have similar shift of absorption edge after adsorption of Sr^{2+} or Cs^{+}. The decrease in the band gap tends to show adsorption may affect chemical environment around the WO_6 octahedron. As shown in Fig. 4, the intensity of peak at ~1400 cm^{-1} is decrease after adsorption of Cs^{+} or Sr^{2+} ions. Adsorption may be an ion exchange process accompanied by exclusion of water, which lead to the more extensive communication of electrons between MO_6 octahedron. So, WO_3 with adsorption of Sr^{2+} or Cs^{+} has a narrower band gap. The difference in the absorption edge energies presented above reflects the differences in bonding between NbO_6 and WO_6 octahedron.

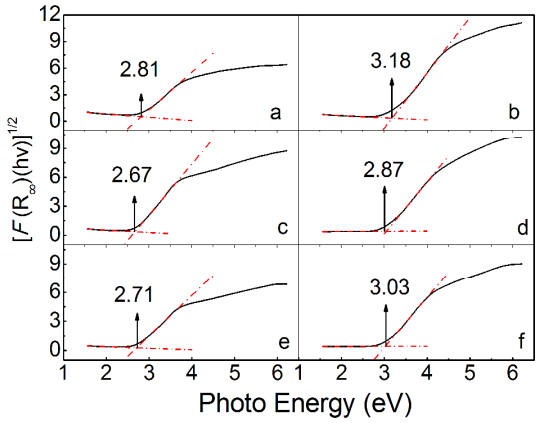

Figure 5 Absorption edge energies are determined by Kubelka-Munk function. hex-WO_3(a), Nb-doped WO_3 (b), Cs adsorbed hex-WO_3(c), Cs adsorbed Nb-doped WO_3(d), Sr adsorbed hex-WO_3(e), Sr adsorbed Nb-doped WO_3(f)

3.6 XPS binding spectroscopy

The XPS spectra of WO_3 samples show two sharp peaks corresponding to W4$f_{7/2}$ and W4$f_{5/2}$

RSC Advances Accepted Manuscript

respectively, indicating W^{6+} oxidation state (Fig.6). No further peaks corresponding to other tungsten oxidation states can be discriminated. Energy shift was encountered after adsorption of Cs^{+} or Sr^{2+}. The first possibility of energy shift was to consider changes in oxidation state. It is well known that there are many oxidation states for W. However, even the lowest binding energy obtained is well within the range normally attributed to W^{6+}. Therefore, the chemical shifts must be explained in terms of the chemical environment around the W centers. It was noticed that XPS spectra of the WO_3 with high hydration have higher binding energy. Vice versa, those with low hydration have intermediate binding energy. So, we were of the opinion that adsorption was an ion exchange process to replace some water molecular in the tunnel of WO_3 [14,15]. As observed by the spectrophotometry data presented above, incorporation of Nb into WO_3 framework is accompanied by water exclusion. Therefore, Nb-doped samples had the lowest energy shift after adsorption of Sr^{2+} or Cs^{+}, comparing to bare hex-WO_3.

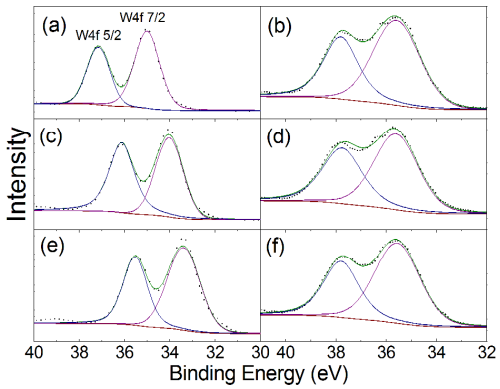

Fig.6 XPS spectra of the W_{4f} core level region for hex-WO_3(a), Nb-doped WO_3 (b), Cs adsorbed hex-WO_3(c), Cs adsorbed Nb-doped WO_3(d), Sr adsorbed hex-WO_3(e), Sr adsorbed Nb-doped WO_3(f)

3.7 Adsorption properties

3.7.1 Effect of Nb doping

The effect of varying Nb dopant concentrations on Sr^{2+} and Cs^{+} adsorption is shown in Fig. 7. Increasing Nb concentration results in increasing Sr^{2+} and Cs^{+} adsorption compared with that of bare *hex*-WO_3. Optimum dopant concentrations occur at Nb/W mole ratio of 0.18~0.24. This may be explained by the fact that crystallinity degrades when Nb is progressively added as observed by

RSC Advances Accepted Manuscript

XRD and SEM. As a result, incorporating too much Nb can lead to collapse of hexagonal tungsten bronze structure and reduce adsorption capacity.

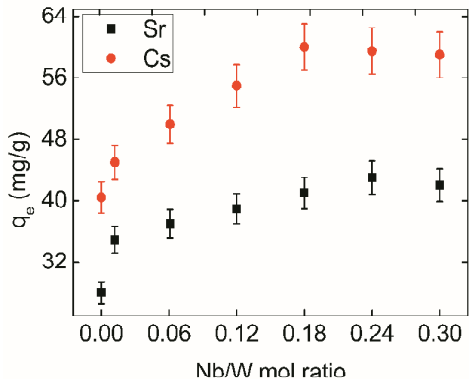

Figure 7 Effect of Nb dopant concentrations on Sr^{2+} and Cs^{+} adsorption. Initial concentration of Cs^{+}=130mg/L, initial concentration of Sr^{2+}=90mg/L, pH=4.

3.7.2 Effect of pH

The pH has a major effect on the adsorption (Fig. 8). The adsorption capacity of Sr^{2+} and Cs^{+} increased gradually with the increasing pH. This trend is in good agreement with the decrease of Zeta potential of Nb-WO_3. These findings demonstrate the presence of a negatively charged is likely to promote adsorption of Sr^{2+} and Cs+. The adsorption of Sr^{2+} and Cs^{+} below pH 4 is lower than expected. Although capacity of adsorption is restrained at low pH, about 40% of Sr^{2+} and Cs^{+} from the initial solution is still extracted even with an HNO_3 concentration of 1 mol·L^{-1}. There are few conventional inorganic adsorbents that can tolerate such high acidity without decomposing, which shows the potential of this sorbent to treat strongly acidic waste.

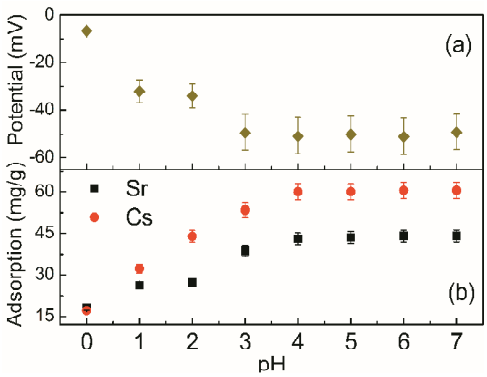

Fig. 8 Effect of pH on Zeta potential (a) and adsorption of Sr^{2+} and Cs^{+} onto Nb-doped WO_3 (b). Initial concentration of Cs^{+}=130mg/L, initial concentration of Sr^{2+}=90mg/L

RSC Advances Accepted Manuscript

3.7.3 Adsorption kinetics

The adsorption capacity of Sr^{2+} and Cs^{+} on the Nb-doped WO_3 increases rapidly with increasing contact time, and then levels off to reach equilibrium within 3 h, as shown in Fig. 9. Best-fit values of q_e, k_1, k_2 and Adj. R^2 for the two models are shown in Table 1. The results showed that the adsorption system followed pseudo-second-order kinetic model for the entire adsorption period, with Adj. R^2 higher than 0.99 for the concentration range used in this study. The q_e calculated values from the model were also consistent with experimental data. The results suggested that the pseudo-second order sorption mechanism was predominant, and that the overall rate of sorption process appeared to be controlled by the chemisorption process.

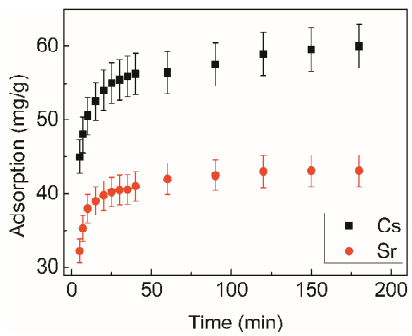

Figure 9 Effect of contact time on adsorption capacity. Initial concentration of Cs^{+}=130mg/L, initial concentration of Sr^{2+}=90mg/L

Table 1 the parameters evaluated from different kinetic models

Model	Parameters	Cs^{+}	Sr^{2+}
Experimental	q_e (mg·g^{-1})	60	43
pseudo-first order	k_1 (min^{-1})	0.018	0.027
	q_e (mg·g^{-1})	9.75	5.86
	Adj. R^2	0.92	0.91
pseudo-second order	k_2 (min^{-1})	0.006	0.012
	q_e (mg·g^{-1})	60.53	43.46
	Adj. R^2	1	1

RSC Advances Accepted Manuscript

3.7.4 Diffusion

The values of *Bt* were plotted against time are shown in Fig. 10. According to Boyd's opinion, the linearity of this plot will provide useful information for distinguishing between film diffusion and intra-particle diffusion rates of sorption [24]. If the plot is a straight line passing through the origin, then sorption will be governed by a particle-diffusion mechanism, otherwise governed by film diffusion. The results indicated that mating plots are linear but fitted poorly, and deviate from origin, suggesting that film diffusion also governed the rate-limiting process. It was noted that the adsorption capacity of Sr^{2+} and Cs^{+} increased gradually with the decrease of Zeta potential of WO_3. All these observations supported the idea that adsorption rate of Sr^{2+} and Cs^{+} on the Nb-doped WO_3 not only involves internal transport mechanisms at low concentration and external transport at higher concentration, but also that the mechanism could be due to electrostatic interactions between the material surface and the ions.

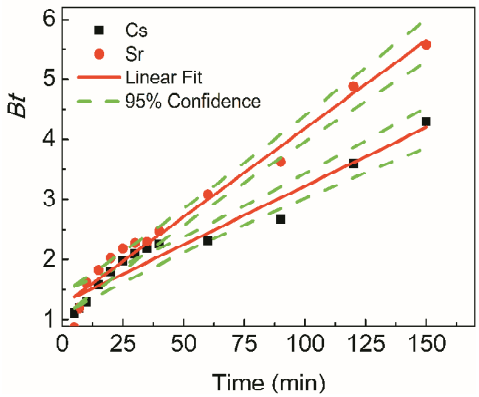

Figure 10 *Bt* plotted against time for the adsorption of Cs^{+} and Sr^{2+} on the Nb-doped WO_3

3.7.5 Adsorption isotherms

The Langmuir and Freundlich isotherm plots for the adsorption of Cs^{+} and Sr^{2+} are shown in Fig. 11. Parameters estimated from the fitted lines are shown in Table 2. It seems that Freundlich isotherm curves fit more reasonable to the adsorption data. Freundlich isotherm is the earliest known relationship describing the non-ideal and reversible adsorption, not restricted to the

RSC Advances Accepted Manuscript

formation of monolayer. This empirical model can be applied to multilayer adsorption, with non-uniform distribution of adsorption heat and affinities over the heterogeneous surface. The amount adsorbed is the summation of adsorption on all sites (each having bond energy), with the stronger binding sites are occupied first, until adsorption energy are exponentially decreased upon the completion of adsorption process. Because of this, it is usually unsatisfactory for high coverage situations. Many results of van der Waals adsorption experiments are adequately expressed by the Freundlich equation, particularly at mid-range concentrations. The magnitude of $1/n$ is generally 0~1, and reflects the exchange intensity or surface heterogeneity. Whereas, a value below unity implies chemisorption process where $1/n$ above one is an indicative of cooperative adsorption. The bonding affinities of Sr^{2+} and Cs^{+} are 0.11 and 0.13 $L \cdot g^{-1}$, respectively. The values of adsorption intensity 1/n<<1 reveal the chemisorption process.

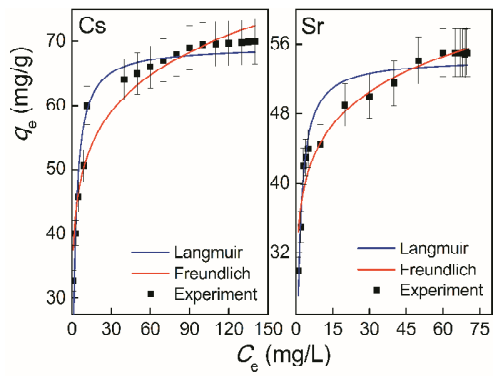

Figre 11 Adsorption equilibrium data for fitted to the Langmuir and Freundlich isotherm models. Initial concentration of Cs^{+},60~280mg/L, initial concentration of Sr^{2+}, 60~180mg/L.

Table 2 Parameters for adsorption isotherm data fitted to the Langmuir and Freundlich models

Model	Parameters	Cs^{+}	Sr^{2+}
Langmuir	Q ($mg \cdot g^{-1}$)	69.33	54.39
	b ($L \cdot mg^{-1}$)	0.51	0.99
	SSE	0.112	0.036
Freundlich	k_f($mg \cdot g^{-1}$)	37.51	34.52
	n	7.50	8.93
	SSE	0.053	0.041

RSC Advances Accepted Manuscript

Conclusion

To search new adsorbents for deal with radioactive waste, extensive series of Nb-doped WO_3 were hydrothermal synthesized in the same condition, which allows a direct comparison of their adsorption properties. The results of batch experiments indicate the adsorption capacity of Sr^{2+} and Cs^{+} onto Nb-doped WO_3 were obviously improved, comparing to bare hex-WO_3. A further proper comparison would be required to test selectivity, capacity, stability, and kinetics of Nb-doped WO_3 and other materials under identical experimental conditions.

Acknowledgements

The authors thank the National Natural Science Foundation of China (Grant No. 41103077) and China Academy of Engineering Physics for financial support.

References

[1] P.A. Kharecha, J.E. Hansen, Prevented Mortality and Greenhouse Gas Emissions from Historical and Projected Nuclear Power, Environ. Sci. Technol., 47 (2013) 4889-4895.

[2] A.M. El-Kamash, Evaluation of zeolite A for the sorptive removal of Cs^{+} and Sr^{2+} ions from aqueous solutions using batch and fixed bed column operations, J. Hazard. Mater., 151 (2008) 432-445.

[3] X. Li, B. Liu, Y. Jian, W. Zhong, W. Mu, J. He, Z. Ma, G. Liu, S. Luo, Ion-Exchange Characteristics of a Layered Metal Sulfide for Removal of $Sr^{2+}$from Aqueous Solutions, Sep. Sci. Technol., 47 (2012) 896-902.

[4] J.L. Mertz, Z.H. Fard, C.D. Malliakas, M.J. Manos, M.G. Kanatzidis, Selective Removal of Cs^{+}, Sr^{2+}, and Ni^{2+} by $K_{2x}Mg_xSn_{3-x}S_6$(x= 0.5–1) (KMS-2) Relevant to Nuclear Waste Remediation, Chem. Mater., 25 (2013) 2116-2127.

[5] A. Tripathi, D.G. Medvedev, M. Nyman, A. Clearfield, Selectivity for Cs and Sr in Nb-substituted titanosilicate with sitinakite topology, J. Solid State Chem., 175 (2003) 72-83.

[6] A.J. Celestian, J.D. Kubicki, J. Hanson, A. Clearfield, J.B. Parise, The Mechanism Responsible for Extraordinary Cs Ion Selectivity in Crystalline Silicotitanate, J. Am. Chem. Soc., 130 (2008) 11689-11694.

[7] D.J. Yang, Z.F. Zheng, H.Y. Zhu, H.W. Liu, X.P. Gao, Titanate Nanofibers as Intelligent Absorbents for the Removal of Radioactive Ions from Water, Adv. Mater., 20 (2008) 2777-2781.

RSC Advances Accepted Manuscript

[8] V. Luca, C.S. Griffith, M.G. Blackford, J.V. Hanna, Structural and ion exchange properties of nanocrystalline Si-doped antimony pyrochlore, J. Mater. Chem., 15 (2005) 564-572.

[9] H. Yang, L. Sun, J. Zhai, H. Li, Y. Zhao, H. Yu, In situ controllable synthesis of magnetic Prussian blue/graphene oxide nanocomposites for removal of radioactive cesium in water, J. Mater. Chem. A, 2 (2014) 326-332.

[10] T. Moller, R. Harjula, M. Pillinger, A. Dyer, J. Newton, E. Tusa, S. Amin, M. Webb, A. Araya, Uptake of ^{85}Sr, ^{134}Cs and ^{57}Co by antimony silicates doped with Ti^{4+}, Nb^{5+}, Mo^{6+} and W^{6+}, J. Mater. Chem., 11 (2001) 1526-1532.

[11] C. Delchet, A. Tokarev, X. Dumail, G. Toquer, Y. Barre, Y. Guari, C. Guerin, J. Larionova, A. Grandjean, Extraction of radioactive cesium using innovative functionalized porous materials, RSC Advances, 2 (2012) 5707-5716.

[12] K. Lv, Y.-M. Luo, L.-P. Xiong, Studies on ion exchange behavior of cesium into zirconium molybdopyrophosphate and its application as precursor of cesium ion sieve, Colloids Surf. A, 417 (2013) 243-249.

[13] K. Lv, L.-P. Xiong, Y.-M. Luo, Ion exchange properties of cesium ion sieve based on zirconium molybdopyrophosphate, Colloids Surf. A, 433 (2013) 37-46.

[14] A. Phuruangrat, D.J. Ham, S.J. Hong, S. Thongtem, J.S. Lee, Synthesis of hexagonal WO_3 nanowires by microwave-assisted hydrothermal method and their electrocatalytic activities for hydrogen evolution reaction, J. Mater. Chem., 20 (2010) 1683-1690.

[15] M.S. Whittingham, Hydrogen motion in oxides: from insulators to bronzes, Solid State Ionics, 168 (2004) 255-263.

[16] X. Li, W. Mu, B. Liu, W. Zhong, H. Wei, Y. Jian, Z. Zhong, S. Luo, S. Li, Adsorption kinetic, isotherm and thermodynamic studies of Sr^{2+} onto hexagonal tungsten oxide, J. Radioanal. Nucl. Chem., 298 (2013) 47-53.

[17] X. Li, W. Mu, X. Xie, B. Liu, H. Tang, G. Zhou, H. Wei, Y. Jian, S. Luo, Strontium adsorption on tantalum-doped hexagonal tungsten oxide, J. Hazard. Mater., 264 (2014) 386-394.

[18] C.S. Griffith, V. Luca, Ion-Exchange Properties of Microporous Tungstates, Chem. Mater., 16 (2004) 4992-4999.

[19] C.S. Griffith, V. Luca, J.V. Hanna, K.J. Pike, M.E. Smith, G.S. Thorogood, Microcrystalline hexagonal tungsten bronze. 1. Basis of ion exchange selectivity for cesium and strontium, Inorg.

RSC Advances Accepted Manuscript

Chem., 48 (2009) 5648-5662.

[20] H.Y. Chang, T. Sivakumar, K.M. Ok, P.S. Halasyamani, Polar Hexagonal Tungsten Bronze-Type Oxides: $KNbW_2O_9$, $RbNbW_2O_9$, and $KTaW_2O_9$, Inorg. Chem., 47 (2008) 8511-8517.

[21] K. Dey, T. Debnath, C. Rüscher, M. Sundberg, A. Hussain, Synthesis and characterization of niobium doped hexagonal tungsten bronze in the systems, $Cs_xNbyW_{1-y}O_3$, J. Mate. Sci., 46 (2011) 1388-1395.

[22] T. Debnath, S. Roy, C. Rüscher, A. Hussain, Synthesis and characterization of niobium-doped potassium tetragonal tungsten bronzes, $K_xNb_yW_{1-y}O_3$, J. Mater. Sci., 44 (2009) 179-185.

[23] Y.S. Ho, G. McKay, The kinetics of sorption of divalent metal ions onto sphagnum moss peat, Water Res., 34 (2000) 735-742.

[24] G.E. Boyd, A.W. Adamson, L.S. Myers, The Exchange Adsorption of Ions from Aqueous Solutions by Organic Zeolites. II. Kinetics, J. Am. Chem. Soc., 69 (1947) 2836-2848.

[25] D. Reichenberg, Properties of Ion-Exchange Resins in Relation to their Structure. III. Kinetics of Exchange, J. Am. Chem. Soc., 75 (1953) 589-597.

[26] A. Hussain, A. Ul-Monir, M.M. Murshed, C.H. Rüscher, Synthesis and Characterization of Niobium Substituted Hexagonal Tungsten Bronzes, Z. Anorg. Allg. Chem., 628 (2002) 416-420.

[27] M. Maczka, J. Hanuza, S. Kojima, A. Majchrowski, J.H. van der Maas, Vibrational spectra of $KNbW_2O_9$ hexagonal tungsten bronze, J. Raman Spectros., 32 (2001) 287-291.

[28] M. Kunz, I.D. Brown, Out-of-Center Distortions around Octahedrally Coordinated d0 Transition Metals, J. Solid State Chem., 115 (1995) 395-406.

[29] W.-J. Chen, C.-F. Zhang, X.-H. Zhang, Y.-F. Zhang, X. Huang, Computational study on the molecular structures and photoelectron spectra of bimetallic oxide clusters $MW_2O_9^{-/0}$ (M=V, Nb, Ta), Spectrochim. Acta, Part A, 109 (2013) 125-132.

[30] E.A. Davis, N.F. Mott, Conduction in non-crystalline systems V. Conductivity, optical absorption and photoconductivity in amorphous semiconductors, Philos. Mag., 22 (1970) 0903-0922.

[31] J. Tauc, R. Grigorovici, A. Vancu, Optical Properties and Electronic Structure of Amorphous Germanium, Phys. Status Solidi B, 15 (1966) 627-637.

[32] F. Urbach, The Long-Wavelength Edge of Photographic Sensitivity and of the Electronic Absorption of Solids, Phys. Rev., 92 (1953) 1324-1324.

[33] K.M. Ok, P.S. Halasyamani, D. Casanova, M. Llunell, P. Alemany, S. Alvarez, Distortions in

RSC Advances Accepted Manuscript

Octahedrally Coordinated d^0 Transition Metal Oxides: A Continuous Symmetry Measures Approach, Chem. Mater., 18 (2006) 3176-3183.

[34] P.S. Halasyamani, Asymmetric Cation Coordination in Oxide Materials: Influence of Lone-Pair Cations on the Intra-octahedral Distortion in d^0 Transition Metals, Chem. Mater., 16 (2004) 3586-3592.

[35] J.M. Poblet, X. Lopez, C. Bo, Ab initio and DFT modelling of complex materials: towards the understanding of electronic and magnetic properties of polyoxometalates, Chem. Soc. Rev., 32 (2003) 297-308.

[36] K.R. Hall, L.C. Eagleton, A. Acrivos, T. Vermeulen, Pore- and Solid-Diffusion Kinetics in Fixed-Bed Adsorption under Constant-Pattern Conditions, Ind. Eng. Chem. Fundam., 5 (1966) 212-223.

RSC Advances Accepted Manuscript